The cellular NMD pathway restricts Zika virus infection and is targeted by the viral capsid protein

Fontaine KA[1], Leon KE[1,2], Khalid MM[1], Jimenez-Morales D[1,3], Tomar S[1], Dunlap M[1], Kaye JA[1], Shah PS[3,6], Finkbeiner S[1,4], Krogan NJ[1,3] and Ott M[1,5].

[1]Gladstone Institutes, San Francisco, CA, [2]Medical Scientist Training Program, University of California, San Francisco, CA, [3]Quantitative Biology Institute, Department of Cellular and Molecular Pharmacology, University of California, San Francisco, CA, [4]Department of Neurology and Physiology, University of California, San Francisco, CA, [5]Department of Medicine, University of California, San Francisco, CA

[6]Present address: Departments of Chemical Engineering and Microbiology and Molecular Genetics, University of California, Davis, CA

Abstract

Zika virus (ZIKV) infection of neural progenitor cells (NPCs) *in utero* is associated with neurological disorders, such as microcephaly[1-3], but a detailed molecular understanding of ZIKV-induced pathogenesis is lacking. Here we show that *in vitro* ZIKV infection of human cells, including NPCs, causes disruption of the nonsense-mediated mRNA decay (NMD) pathway. NMD is a cellular mRNA surveillance mechanism that is required for normal brain size in mice[4-6]. Using affinity purification-mass spectrometry, we identified multiple cellular NMD factors that bind to the viral capsid protein, including the central NMD regulator up-frameshift protein 1 (UPF1)[7]. Endogenous UPF1 interacted with the viral capsid protein in co-immunoprecipitation experiments, and capsid expression post-transcriptionally downregulated UPF1, a process that we confirmed occurs during *de*

novo **ZIKV infection. A further decrease in UPF1 levels by RNAi significantly enhanced ZIKV infection in NPC cultures. RNA electrophoretic mobility shift assays with UPF1-expressing cell lysates showed binding to ZIKV RNA *in vitro*, and UPF1 protein in ZIKV-infected NPCs colocalized with viral double-stranded RNA replication intermediates. Collectively, our data support a model where ZIKV, via the capsid protein, has evolved a strategy to dampen antiviral activities of NMD[8,9], which subsequently contributes to neuropathology *in vivo.***

Main

ZIKV is a mosquito-borne RNA virus that belongs to the *Flaviviridae* family. First isolated in Uganda in 1947, ZIKV remained relatively obscure for decades following its discovery because infection was associated with only mild disease. However, more severe clinical manifestations, including microcephaly, have been observed during the recent spread of ZIKV through the Americas[10]. While it is now established that ZIKV infection during pregnancy is a causative agent of microcephaly[11], the molecular mechanisms underlying ZIKV-induced neuropathogenesis remain largely unknown.

Microcephaly has been linked to genetic mutations that result in the impairment of the NMD pathway[4-6]. While NMD was initially found to serve as a quality control system that destroys transcripts containing premature termination codons, the pathway also targets a broader range of RNA substrates, including viral RNAs[7-9,12,13]. As ZIKV has an RNA genome, and we previously described perturbations of the NMD pathway in cells infected with hepatitis C virus[14], we hypothesized that ZIKV infection manipulates the cellular NMD pathway.

To determine if ZIKV infection affects NMD, we infected human hepatic cells (the Huh7 cell line) and human induced pluripotent stem cell (iPSC)-derived NPCs, two relevant target cell types, with ZIKV for 48 h. We isolated total RNA from infected cells and measured mRNA levels of three canonical NMD substrates: asparagine synthetase (ASNS), cysteinyl-tRNA synthetase

(CARS), and SR protein SC35[14]. ASNS, CARS, and SC35 transcripts were significantly elevated in Huh7 cells and NPCs following infection with Asian lineage ZIKV strain P6-740 (Fig. 1a). Levels of NMD substrates were also elevated in Huh7 cells infected with the contemporary ZIKV clinical isolate PRVABC59 (Puerto Rico, 2015)(Fig. 1a). We found that ZIKV-induced increase in NMD transcripts did not reflect a global increase in transcription, as mRNA levels of housekeeping genes, including glyceraldehyde 3-phosphate dehydrogenase (GAPDH), were not altered in infected cells (Fig. 1a). Together, these results indicate that ZIKV disrupts the NMD pathway during infection.

NMD substrates are regulated through the activity of UPF1, an evolutionarily conserved ATP-dependent RNA helicase. UPF1 plays a central role in the NMD pathway by linking the translation termination event to the assembly of a surveillance complex, resulting in NMD activation[15]. To determine if ZIKV infection more broadly affects NMD, we utilized two publicly available RNA sequencing (RNA-Seq) datasets to compare genome-wide transcriptional alterations found during ZIKV infection[16] to those found following UPF1 knockdown[17]. As shown in Figure 1b, there is a significant overlap in upregulated genes between these two datasets. Interestingly, several of the overlapping genes are involved in cell cycle arrest and induction of apoptosis, two conditions linked to ZIKV-associated neuropathology[1]. These genes include DNA damage-inducible transcript 3 (DDIT3)[18] and growth arrest and DNA damage-inducible protein 45 alpha and beta (GADD45A and GADD45B, respectively)[19]. Via quantitative real-time RT-PCR, we confirmed that transcripts of each were upregulated following infection of Huh7 cells with ZIKV PRVABC59, while the mRNA levels of the housekeeping genes GAPDH, hypoxanthine phosphoribosyltransferase 1 (HPRT1), and lactate dehydrogenase A (LDHA) were not elevated (Fig. 1c). Combined, these data show that ZIKV infection is associated with dysregulated expression of NMD substrates relevant to ZIKV-mediated neuropathogenesis.

We previously showed that the core protein of HCV and capsid protein of the related flaviviruses dengue virus and West Nile virus interact with within bgcn homolog (WIBG/PYM1),

a component of the exon junction complex (EJC) associated with NMD[14]. To examine potential interactions between ZIKV and the NMD pathway, we separately analyzed data generated from an affinity purification-mass spectrometry (AP-MS) screen to specifically query whether the capsid protein of ZIKV interacts with NMD-associated host factors (Shah et al., submitted). ZIKV-host protein-protein interaction (PPI) maps were generated in HEK293T cells using ZIKV proteins from the Ugandan 1947 strain MR 766 or the French Polynesian 2013 strain H/PF/2013 as bait proteins. From this analysis, we found that ZIKV capsid proteins interacted with several factors of the NMD pathway, including multiple members of the EJC complex, as well as UPF1 and UPF3B (UPF3B is an NMD effector that stimulates the helicase activity of UPF1) (Fig. 2a). Importantly, the NMD host factors that interact with each of the two different capsid proteins greatly overlapped, revealing that the interaction between capsid and the NMD pathway is conserved across the Asian and African lineages of ZIKV (Fig. 2a).

Next, we validated the binding of ZIKV capsid to UPF proteins by co-immunoprecipitating Flag-tagged capsid protein with endogenous UPF3B or UPF1 in HEK293T cells. Both UPF3B and UPF1 proteins co-immunoprecipitated with ZIKV capsid, confirming the AP-MS results (Fig. 2b,c, respectively). In addition, ZIKV capsid colocalized with endogenous UPF1 in transfected Huh7-Lunet cells, as visualized and quantified by confocal immunofluorescent microscopy and three-dimensional (3D) reconstruction analysis (Mander's colocalization coefficient of ~57%) (Fig. 2d).

Surprisingly, we consistently observed a decrease in UPF1, but not UPF3B, protein levels in the input lysate of ZIKV capsid-transfected cells, pointing to a specific perturbation of UPF1 expression by ZIKV capsid (Fig. 2c). To confirm that UPF1 protein levels are dysregulated during *de novo* ZIKV infection, we performed western blot analysis of infected Huh7 cells and NPCs. Cellular UPF1 protein levels were consistently downregulated by ~50% in ZIKV-infected Huh7 cells, whereas a ~25% reduction was observed in ZIKV-infected NPCs (Fig. 3a,b, respectively). This difference in UPF1 downregulation mirrors the difference in infection

efficiencies achieved in these two cell systems. UPF1 transcript levels were not decreased in ZIKV-infected cells or following capsid overexpression, suggesting that UPF1 is post-transcriptionally downregulated during ZIKV infection (Fig. 3c,d, respectively).

We hypothesized that UPF1 serves as a restriction factor of ZIKV and is inactivated in infected cells to promote ZIKV propagation. To test this hypothesis, we decreased UPF1 expression prior to ZIKV infection by transfecting NPCs with either non-targeting siRNA or a pool of UPF1-specific siRNAs. We then infected the transfected cells with ZIKV and measured viral RNA levels, as well as infectious titers, 48 h post-infection (hpi). UPF1 knockdown was successful in siRNA-treated cells, as confirmed by western blot analysis (Fig. 4a). The depletion of UPF1 in NPCs prior to infection resulted in a significant increase in both ZIKV RNA levels and infectious virus production (Fig. 4b,c respectively), supporting the model that expression of UPF1 restricts ZIKV infection at or before the RNA replication stage. During viral RNA replication, double-stranded RNA (dsRNA) intermediates are generated, which can be visualized with a specific antibody[20]. Using confocal microscopy and 3D reconstruction analyses, we observed no significant difference in the number and size of dsRNA foci when we compared ZIKV-infected, UPF1-depleted NPCs to ZIKV-infected cells expressing UPF1 (Supplemental Fig. 1). Instead, we found a significant increase in the number of infected cells in NPC cultures when UPF1 was depleted, underscoring that UPF1 expression affects the permissivity of NPCs to ZIKV infection (Fig. 4d), Interestingly, endogenous UPF1 colocalized with viral dsRNA with ~54% of the 3D-reconstructed RNA replication loci also scoring positive for UPF1 fluorescence, indicating that UPF1 targets ZIKV at the RNA replication stage (Fig. 4e). Furthermore, a chemiluminescent RNA electrophoretic mobility shift assay (EMSA) with cell lysates and full-length biotinylated ZIKV RNA resulted in a marked shift in ZIKV RNA gel migration that was significantly enhanced when UPF1 was overexpressed (Fig. 4f). Combined, these data support a model where UPF1, together with its cellular partners, directly targets ZIKV RNA possibly rendering it for destruction. Of note, we observed several faster migrating RNA-

protein complexes in these assays, especially when UPF1 was overexpressed, but further studies are needed to conclusively show UPF1-dependent processing of ZIKV RNA.

In summary, we identified the NMD pathway as a restriction mechanism for ZIKV infection in human NPCs. NMD was partially inactivated in ZIKV-infected NPCs through expression of the viral capsid protein and the resulting downregulation of host UPF1 protein levels. As further weakening NMD by depleting UPF1 results in a marked increase in the number of infected cells, we propose a model in which an “arms race” between cellular NMD and ZIKV determines whether a cell is successfully infected (Figure 4g). The downregulation of UPF1 by capsid during ZIKV infection may be limited by toxic effects of NMD impairment, as illustrated by the upregulation of genes involved in cell cycle growth arrest and apoptosis. Indeed, ZIKV-induced NMD impairment may contribute to severe neuropathology and microcephaly development, as documented in mice haploinsufficient for NMD factors[4-6]. Studies are ongoing to determine the precise molecular mechanisms of ZIKV capsid-induced UPF1 downregulation and the processing of ZIKV RNA by cellular NMD. This research may lead to new therapeutic approaches, as reinforcement of the antiviral properties of the NMD pathway is expected to enhance resistance of NPCs to ZIKV infection and could promote normal neurodevelopment in infected fetuses.

Methods

Viruses and cells. Two Asian lineage strains of ZIKV, P6-740 (ATCC VR-1845) and PRVABC59 (ATCC VR-1843), were used for all experiments. ZIKV stocks were propagated in Vero cells (ATCC) and titers were determined by plaque assays on Vero cells. Huh7 cells (ATCC), Huh7-Lunet cells (Ralf Bartenschlager, Heidelberg University) and Vero cells were maintained in Dulbecco’s Modified Eagle’s Medium (DMEM) with 10% fetal bovine serum (FBS), 2 mM L-glutamine, 100 U/mL penicillin, and 100 µg/mL streptomycin. HEK293T cells (ATCC) were maintained in DMEM/H21 medium supplemented with 10% FBS, 100 U/mL penicillin, 100

157 µg/mL streptomycin, and 1 mM sodium pyruvate or DMEM with 10% FBS, 2 mM L-glutamine,
158 100 U/mL penicillin, and 100 µg/mL streptomycin. Human iPSC-derived NPCs were generated
159 and maintained as described previously[21]. All of the human fibroblast cell lines used to generate
160 iPSCs came from the Coriell Institute for Medical Research and Yale Stem Cell Center. The
161 iPSCs used in these studies were the CTRL2493nXX, CS2518nXX, and Cs71iCTR-20nXX
162 lines. CTRL2493nXX was derived from the parental fibroblast line ND31845 that was biopsied
163 from a healthy female at 71 years of age. CS2518nXX was derived from the parental fibroblast
164 line ND30625 that was biopsied from a healthy male at 76 years of age. CS71iCTR-20nXX was
165 derived from the parental fibroblast line ND29971 that was biopsied from a female at 61 years of
166 age. For virus infections, NPCs plated on Matrigel-coated (Corning) multi-well plates or Huh7
167 cells were infected with ZIKV at a multiplicity of infection (MOI) of 0.1 or 1 for 2 h at 37°C.
168 Infected cells were harvested at 48 hpi for all analyses.
169
170 **Affinity purification, mass spectrometry, and AP-MS scoring.** The ZIKV capsid open
171 reading frames (ORFs) from the Ugandan 1947 strain MR 766 or the French Polynesian 2013
172 strain H/PF/2013 were cloned into pCDNA4_TO with a C-terminal 2xStrep II affinity tag for
173 expression in human cells. The viral capsid proteins (three biological replicates), as well as GFP
174 (two biological replicates) and empty vector (ten biological replicates) as negative controls, were
175 expressed in HEK293T cells and affinity purifications were performed as previously described[22].
176 All lysates and affinity purified eluates were analyzed by western blot and silver stain PAGE to
177 confirm expression and purification. Purified protein eluates were digested with trypsin for LC-
178 MS/MS analysis. Samples were denatured and reduced in 2M urea, 10 mM NH_4HCO_3, 2 mM
179 DTT for 30 min at 60°C, then alkylated with 2 mM iodoacetamide for 45 min at room
180 temperature. Trypsin (Promega) was added at a 1:100 enzyme:substrate ratio and digested
181 overnight at 37°C. Following digestion, samples were concentrated using C18 ZipTips

(Millipore) according to the manufacturer's specifications. Peptides were resuspended in 15 µL of 4% formic acid and 3% ACN, and 1-2 µL of sample was loaded onto a 75 µm ID column packed with 25 cm of Reprosil C18 1.9 µm, 120Å particles (Dr. Maisch). Peptides were eluted into a Q-Exactive Plus (Thermo Fisher) mass spectrometer by gradient elution delivered by an Easy1200 nLC system (Thermo Fisher). The gradient was from 4.5% to 32% acetonitrile over 53 minutes. All MS spectra were collected with oribitrap detection, while the 20 most abundant ions were fragmented by HCD and detected in the orbitrap. All data was searched against the SwissProt Human protein sequences, combined with ZIKV sequences and GFP. Peptide and protein identification searches, as well as label-free quantitation, were performed using the MaxQuant data analysis algorithm and all peptide and protein identifications were filtered to a 1% false-discovery rate[23, 24]. SAINTq[25] was used to calculate the probability of bait-prey interactions for both Ugandan ZIKV capsid and French Polynesian ZIKV capsid against the negative controls, including GFP and empty vector, with protein intensities as input values. We applied a combined threshold of probability of interaction (AvgP) greater than 0.90 and Bayesian False Discovery Rate of less than 0.05.

Quantitative real-time reverse transcription-PCR (qRT-PCR). Total cellular RNA was isolated from Huh7 cells and NPCs using the RNeasy Mini Kit (Qiagen). cDNA was synthesized with oligo$(dT)_{18}$ (ThermoFisher Scientific) primers, random hexamer (Life Technologies) primers, and AMV reverse transcriptase (Promega). The cDNA was then used in SYBR Green PCR Master Mix (ThermoFisher Scientific) according to manufacturer's instructions and analyzed by qPCR (Bio-Rad ABI 7900). The primers used for ASNS, CARS, SC35 1.7, GAPDH, HPRT1, LDHA, and 18S rRNA have been described previously[14]. The additional primers used were ZIKV PRVABC59 forward primer 5'- GAG ACG AGA TGC GGT ACA GG -3', ZIKV PRVABC59 reverse primer 5'- CGA CCG TCA GTT GAA CTC CA -3', UPF1 forward primer 5'- CTG CAA CGG ACG TGG AAA TAC -3', UPF1 reverse primer 5'- ACA GCC GCA GTT GTA

GCA C -3', DDIT3 forward primer 5'- CTG CTT CTC TGG CTT GGC TG -3', DDIT3 reverse primer 5'- GCT CTG GGA GGT GCT TGT GA -3', GADD45A forward primer 5'- GAG CTC CTG CTC TTG GAG AC -3', GADD45A reverse primer 5'- GCA GGA TCC TTC CAT TGA GA -3', GADD45B forward primer 5'- TGA CAA CGA CAT CAA CAT C -3', and GADD45B reverse primer 5'- GTG ACC AGA GAC AAT GCA G -3'. Relative levels of each transcript were normalized by the delta threshold cycle method to the abundance of 18S rRNA or GAPDH, with mock-infected cells or vector-transfected cells set to 1.

Western blot analysis. Cells were lysed in RIPA lysis buffer (50mM Tris-HCl, pH 8, 150mM NaCl, 1% NP-40, 0.5% sodium deoxycholate, 0.1% SDS, supplemented with Halt™ protease inhibitor cocktail (ThermoFisher Scientific)) to obtain whole cell lysates or lysed using the NE-PER nuclear and cytoplasmic extraction kit (ThermoFisher Scientific) to obtain cytoplasmic and nuclear fractions. Proteins were separated by SDS-PAGE and transferred to nitrocellulose membranes (Bio-Rad). Blots were incubated with the indicated primary antibody: anti-UPF3B (ab134566, Abcam), anti-UPF1 (12040, Cell Signaling Technology, Inc.), anti-ZIKV Envelope (E) (GTX133314, GeneTex), anti-ZIKV Capsid (C) (GTX133304, GeneTex), anti-Flag (F7425, Sigma-Aldrich), and anti-β-actin (A5316, Sigma-Aldrich). Proteins were visualized by chemiluminescent detection with ECL and ECL Hyperfilm (Amersham). Differences in band intensity were quantified by densitometry using ImageJ.

Immunoprecipitations. Cells were lysed in either RIPA lysis buffer or IP lysis buffer (150mM NaCl, 50mM Tris pH 7.4, 1mM EDTA, 0.5% NP-40 substitute, supplemented with Halt™ protease inhibitor cocktail (ThermoFisher Scientific)) at 4°C and passed through a G23 needle. Clarified lysates were immunoprecipitated with Flag M2 agarose (Sigma) overnight, washed in lysis buffer, and resuspended in Laemmli buffer for SDS-PAGE. Western blot analysis of immunoprecipitated proteins was performed as described above.

Immunofluorescence. Transfected Huh7-Lunet cells or infected NPCs were collected at 48 h and plated onto 22 × 22 mm #1.5 coverslips. Cells were fixed in 4% paraformaldehyde, permeabilized with 0.1% Triton X-100, and blocked in 3% bovine serum albumin. Cells were then immunostained with the indicated antibodies: anti-Strep Tag (Abcam, ab184224), anti-UPF1 (Abcam, ab109363), human anti-DENV mAb 1.6D (a generous gift from Sharon Isern and Scott Michael, Florida Gulf Coast University), which recognizes the ZIKV envelope protein, anti-dsRNA mAb J2 (SCICONS), and the appropriate fluorophore-conjugated secondary antibodies. Coverslips were mounted onto glass slides using Vectashield® Mounting Medium with DAPI (Vector Laboratories) and analyzed by fluorescence microscopy (Zeiss Axio Observer ZI) or confocal microscopy (Zeiss LSM 880). For acquiring high-resolution images, cells were imaged on the Zeiss LSM 880 with Airyscan using a 20x/0.8 or 63x/1.4 M27 oil immersion objective. A total of 15-20 (20x objective) or 60-80 (63x objective) Z-slices were acquired every 0.88 µm or 0.15 µm, respectively. The resulting Z-stack was reconstructed and rendered in 3D using Imaris software (Bitplane). Viral dsRNA foci were reconstructed via the Imaris spot detection function, which provided an analysis of total number and mean volume of foci within a cell, for images acquired using the 20x objective. Strep-tagged ZIKV capsid, UPF1, and dsRNA channels acquired using the 63x objective were reconstructed using the Imaris surfaces package. The Imaris colocalization function was used to determine overlap of fluorescence. Thresholding for background fluorescence was determined by the Imaris automatic thresholding tool that utilizes the Costes approach[26]. The thresholded Mander's correlation coefficient (MCC) measures the fraction of voxels with fluorescence positive for one channel that also contain fluorescence from another channel. The MCC is typically more appropriate for analysis of three-dimensional colocalization[27].

Chemiluminescent RNA EMSA. The cDNA for the full-length ZIKV genome was generated by ligating two DNA fragments containing the structural and nonstructural genes from a two-

plasmid system (pJW231 and pJW232), as previously described[28]. After ligation, the full-length cDNA was *in vitro* transcribed and biotinylated via the HiScribe™ T7 ARCA mRNA Kit (NEB) and Pierce™ RNA 3' End Biotinylation Kit (ThermoFisher Scientific). RNA EMSA was performed by incubating biotinylated ZIKV RNA with the indicated protein lysates and visualizing RNA-protein complex formation according to manufacturer's instructions (LightShift™ Chemiluminescent RNA EMSA Kit, ThermoFisher Scientific).

Statistical analysis. Statistical differences between groups were analyzed using either a two-tailed unpaired Student's *t*-test or a two-tailed ratio paired Student's *t*-test, as stated in the figure legends. Hypergeometrical tests were used to calculate the probability of an overlap in gene dysregulation between ZIKV-infected NPCs and UPF1-depleted cells and to calculate the probability of ZIKV capsid bait-prey interactions. Data are represented as mean ± s.e.m. Statistical significance was defined as $*P \leq 0.05$, $**P \leq 0.01$, $***P \leq 0.001$, and $****P \leq 0.0001$.

Acknowledgements. The authors would like to thank all members of the Ott laboratory, as well as Roman Camarda and Marius Walter, for helpful discussions and advice throughout the preparation of this manuscript. We thank Chia-Lin Tsou, Mandy Muller (University of Massachusetts, Amherst), the Gladstone Stem Cell Core, and Meredith Calvert from the Gladstone Microscopy Core for technical assistance, and Ralf Bartenschlager (Heidelberg University), Gregory Ebel (Colorado State University), and Sharon Isern and Scott Michael (Florida Gulf Coast University) for reagents. We are grateful to Veronica Fonseca for administrative support, John Carroll and Teresa Roberts for graphical design, and to Eric Martens and Gary Howard for editorial assistance. This work was supported by NIH/NIAID F32AI112262 to P.S.S., NIH/NINDS R01 NS101996-01 to S.F., NIH/NIAID U19AI1186101 to N.J.K., DOD/DARPA HR0011-11-C-0094 (PROPHECY) to N.J.K., NIH/NIAID R01 AI097552 to M.O., and the James B. Pendleton Charitable Trust.

Competing interests. The authors declare no competing financial interests.

Author contributions. K.A.F., K.E.L., M.M.K., and P.S.S. designed, conducted, and analyzed the experiments. D.J. performed the bioinformatics analyses and provided graphical support. M.O. supervised, guided, and funded the project. S.T., M.D., J.A.K., S.F., and N.J.K. provided critical reagents and technical guidance. The manuscript was written by K.A.F., K.E.L., and M.O. with input from N.J.K.

Figure Legends

Figure 1. The NMD pathway is disrupted during ZIKV infection.

(a) Transcript levels of NMD substrates and housekeeping genes from Huh7 cells or NPCs mock-infected or infected with ZIKV strain P6-740 or the contemporary clinical isolate PRVABC59. Cells were infected at a multiplicity of infection (MOI) of 0.1 or 1 and harvested at 48 hpi. Data are represented as mean ± s.e.m. *P* values were calculated by unpaired Student's *t*-test. **P* ≤ 0.05; ***P* ≤ 0.01; ns, not significant. n= 3 independent experiments.

(b) Venn diagram showing overlap of significantly upregulated genes associated with ZIKV infection of NPCs and UPF1 knockdown in HeLa cells. RNA-Seq analyses of mock-infected or ZIKV-infected NPCs harvested at 56 hpi and control siRNA-treated or UPF1 siRNA-treated HeLa TO cells harvested at 72 h post-transfection (hpt). The GeneProf hypergeometric probability calculator (http://www.geneprof.org/GeneProf/tools/hypergeometric.jsp) was then used to generate a hypergeometric *P* value. *****P* ≤ 0.0001.

(c) Transcript levels of housekeeping genes and select genes involved in cell cycle growth arrest and apoptosis that were identified in (b). Huh7 cells were mock-infected or infected with ZIKV PRVABC59 at an MOI of 0.1 or 1 and harvested at 48 hpi. Data are represented as mean

± s.e.m. *P* values were calculated by unpaired Student's *t*-test. **P* ≤ 0.05; ***P* ≤ 0.01; ****P* ≤ 0.001; ns, not significant. n= 3 independent experiments.

Figure 2. The capsid protein of ZIKV interacts with the NMD pathway and downregulates UPF1.

(a) Ugandan ZIKV capsid (Ug Cap, MR 766) and French Polynesian ZIKV capsid (Fp Cap, H/PF/2013) PPI maps that show significant enrichment for host NMD-associated factors (purple), as identified by AP-MS (SAINTq probability score > 0.9 and FDR < 0.05). Ten interactions between Fp Cap and host NMD factors (hypergeometrical test, *P* value = 7.16×10^{-10}) and eight interactions between Ug Cap and host NMD factors (*P* value = 3.45×10^{-7}) were identified.

(b) Co-immunoprecipitation (co-IP) and western blot analysis of HEK293T cells transfected with vector or Flag-tagged ZIKV capsid (H/PF/2013, Asian lineage) and harvested at 48 hpt to immunoprecipitate endogenous UPF3B. The upper band detected in the IP Capsid blot represents a non-specific artifact.

(c) Co-IP and western blot analysis of HEK293T cells transfected with vector or Flag-tagged ZIKV capsid and harvested at 48 hpt to immunoprecipitate endogenous UPF1.

(d) Representative 3D confocal microscopy images of Huh7-Lunet cells transfected with vector or Strep-tagged ZIKV capsid. Cells were processed for immunostaining at 48 hpt and probed with antibodies against Strep-tag (turquoise) and endogenous UPF1 (purple). DAPI (blue) was used to stain the nuclei. Each channel was reconstructed digitally for visualization of the 3D colocalization. The thresholded Mander's correlation coefficient for ZIKV capsid was 0.57 (n = 17), indicating that approximately 57% of the voxels positive for capsid fluorescence were also positive for UPF1 fluorescence. Scale bar represents 5 μm.

Figure 3. UPF1 is post-transcriptionally downregulated during ZIKV infection.

(a) Western blot analysis of UPF1 levels in mock-infected and ZIKV-infected (PRVABC59, MOI of 1) Huh7 cells harvested at 48 hpi, with β-actin and ZIKV envelope protein (ZIKV E) serving as loading and infection controls, respectively. Densitometric analyses were performed using ImageJ to quantify relative band intensities. Data are represented as mean ± s.e.m. *P* values were calculated by unpaired Student's *t*-test. $^{**}P \leq 0.01$. n= 3 independent experiments.

(b) Western blot analysis of UPF1 levels in mock-infected and ZIKV-infected (P6-740, MOI of 1) NPCs harvested at 48 hpi, with β-actin and ZIKV capsid protein (ZIKV C) serving as loading and infection controls, respectively. Densitometric analyses were performed using ImageJ to quantify relative band intensities. Data are represented as mean ± s.e.m. *P* values were calculated by unpaired Student's *t*-test. $^{***}P \leq 0.001$. n= 3 independent experiments using one NPC line.

(c) UPF1 transcript levels from Huh7 cells mock-infected or infected with ZIKV strain PRVABC59 at an MOI of 0.1 or 1 and harvested at 48 hpi. Data are represented as mean ± s.e.m. *P* values were calculated by unpaired Student's *t*-test. ns, not significant. n= 3 independent experiments.

(d) UPF1 transcript levels from HEK293T cells transfected with vector or Strep-tagged ZIKV capsid (H/PF/2013, Asian lineage) and harvested at 48 hpt. Data are represented as mean ± s.e.m. *P* values were calculated by unpaired Student's *t*-test. ns, not significant. n= 3 independent experiments.

Figure 4. UPF1 is a restriction factor of ZIKV.

(a) Western blot analysis of UPF1 levels in NPCs transfected with non-targeting siRNA (siNT) or a pool of UPF1-specific siRNAs (siUPF1) at 96 hpt. Densitometric analyses were performed using ImageJ to quantify relative band intensities. Data are represented as mean ± s.e.m. *P* value was calculated by unpaired Student's *t*-test. $^{**}P \leq 0.01$. n= 3 independent experiments using one NPC line.

(b) ZIKV RNA levels in siNT-treated or siUPF1-treated NPCs infected with ZIKV strain PRVABC59 at an MOI of 0.1 or 1 and harvested at 48 hpi. Data are represented as mean ± s.e.m. *P* value was calculated by two-tailed ratio paired Student's *t*-test. ***$P \leq 0.001$. n= 3 independent experiments using one NPC line.

(c) Released infectious virus from siNT-treated or siUPF1-treated, ZIKV-infected (MOI of 1) NPCs harvested at 48 hpi. Data are represented as mean ± s.e.m. *P* value was calculated by unpaired Student's *t*-test. **$P \leq 0.01$. n= 3 independent experiments using one NPC line.

(d) Infection rates of siNT-treated or siUPF1-treated, ZIKV-infected (MOI of 1) NPCs measured at 48 hpi. Fixed cells were subjected to the anti-DENV mAb 1.6D, which also recognizes the ZIKV envelope protein. Data are represented as mean ± s.e.m. *P* value was calculated by two-tailed ratio paired Student's *t*-test. **$P \leq 0.01$. n = 3 independent experiments using two NPC lines.

(e) Representative 3D confocal microscopy images of mock-infected or ZIKV-infected (MOI of 1) NPCs processed for immunostaining at 48 hpi. Cells were probed with antibodies against dsRNA (teal) and endogenous UPF1 (purple), with DAPI (blue) used to stain the nuclei. Each channel was reconstructed digitally for visualization of the 3D colocalization. The thresholded Mander's correlation coefficient for ZIKV dsRNA was 0.54, indicating that approximately 54% of the voxels positive for dsRNA fluorescence were also positive for UPF1 fluorescence. n = 3 independent experiments using one NPC line, with 4 cells analyzed per condition for each experiment. Scale bar represents 5 μm.

(f) Chemiluminescent RNA EMSA of biotinylated *in vitro* transcribed ZIKV RNA with protein lysate from vector-transfected or UPF1-transfected HEK293T cells in the absence or presence of specific competitor unlabeled ZIKV RNA. Results are representative of at least three independent experiments.

(g) Model of the interaction between the capsid protein of ZIKV and UPF1 of the NMD pathway.

Supplemental Figure 1. ZIKV dsRNA foci number and volume are not altered in UPF1-depleted NPCs.

(a) Representative confocal microscopy images of a ZIKV-infected, siNT-treated NPC or a ZIKV-infected, siUPF1-treated NPC with the nuclei stained with DAPI (blue) and ZIKV dsRNA foci stained with the anti-dsRNA mAb J2 (teal). 3D image rendering and reconstructed dsRNA foci were produced using the Imaris spot detection function. Scale bar represents 2 μm.

(b) Number of dsRNA foci were averaged for each cell. Data are represented as mean ± s.e.m. *P* value was calculated by two-tailed ratio paired Student's *t*-test. ns, not significant. n = 3 independent experiments using two NPC lines, with 3-10 cells analyzed per condition for each experiment.

(c) Measurement of dsRNA foci volume were averaged for each cell. Data are represented as mean ± s.e.m. *P* value was calculated by two-tailed ratio paired Student's *t*-test. ns, not significant. n = 3 independent experiments using two NPC lines, with 3-10 cells analyzed per condition for each experiment.

References

1. Li, C. *et al*. Zika Virus Disrupts Neural Progenitor Development and Leads to Microcephaly in Mice. *Cell Stem Cell* **19**, 120-126 (2016).

2. Cugola, F. R. *et al*. The Brazilian Zika virus strain causes birth defects in experimental models. *Nature* **534**, 267-271 (2016).

3. Miner, J. J. *et al*. Zika Virus Infection during Pregnancy in Mice Causes Placental Damage and Fetal Demise. *Cell* **165**, 1081-1091 (2016).

4. Silver, D. L. *et al*. The exon junction complex component Magoh controls brain size by regulating neural stem cell division. *Nat. Neurosci.* **13**, 551-558 (2010).

5. Mao, H., McMahon, J. J., Tsai, Y., Wang, Z. & Silver, D. L. Haploinsufficiency for Core Exon Junction Complex Components Disrupts Embryonic Neurogenesis and Causes p53-Mediated Microcephaly. *PLoS Genetics* **12**, e1006282 (2016).

6. Mao, H. *et al*. Rbm8a haploinsufficiency disrupts embryonic cortical development resulting in microcephaly. *J. Neurosci.* **35**, 7003-7018 (2015).

7. Brogna, S. & Wen, J. Nonsense-mediated mRNA decay (NMD) mechanisms. *Nature Structural & Molecular Biology* **16**, 107-113 (2009).

8. Jerome M Molleston & Sara Cherry. Attacked from All Sides: RNA Decay in Antiviral Defense. *Viruses* **9**, 2 (2017).

9. Rigby, R. E. & Rehwinkel, J. RNA degradation in antiviral immunity and autoimmunity. *Trends in Immunology* **36**, 179-188 (2015).

10. Fauci, A. S. & Morens, D. M. Zika Virus in the Americas--Yet Another Arbovirus Threat. *N. Engl. J. Med.* **374**, 601-604 (2016).

11. Rasmussen, S. A., Jamieson, D. J., Honein, M. A. & Petersen, L. R. Zika Virus and Birth Defects — Reviewing the Evidence for Causality. *N. Engl. J. Med.* **374**, 1981-1987 (2016).

12. Balistreri, G., Bognanni, C. & Mühlemann, O. Virus Escape and Manipulation of Cellular Nonsense-Mediated mRNA Decay. *Viruses* **9** (2017).

429 13. Balistreri, G. *et al*. The host nonsense-mediated mRNA decay pathway restricts Mammalian
430 RNA virus replication. *Cell Host Microbe* **16**, 403-411 (2014).
431 14. Ramage, H. R. *et al*. A combined proteomics/genomics approach links hepatitis C virus
432 infection with nonsense-mediated mRNA decay. *Mol. Cell* **57**, 329-340 (2015).
433 15. Hug, N., Longman, D. & Cáceres, J. F. Mechanism and regulation of the nonsense-
434 mediated decay pathway. *Nucleic Acids Res.* **44**, 1483-1495 (2016).
435 16. Tang, H. *et al*. Zika Virus Infects Human Cortical Neural Progenitors and Attenuates Their
436 Growth. *Cell Stem Cell* **18**, 587-590 (2016).
437 17. Tani, H. *et al*. Identification of hundreds of novel UPF1 target transcripts by direct
438 determination of whole transcriptome stability. *RNA Biology* **9**, 1370-1379 (2012).
439 18. Jauhiainen, A. *et al*. Distinct cytoplasmic and nuclear functions of the stress induced protein
440 DDIT3/CHOP/GADD153. *PLoS ONE* **7**, e33208 (2012).
441 19. Salvador, J. M., Brown-Clay, J. D. & Fornace, A. J. Gadd45 in stress signaling, cell cycle
442 control, and apoptosis. *Adv. Exp. Med. Biol.* **793**, 1-19 (2013).
443 20. Klema, V. J., Padmanabhan, R. & Choi, K. H. Flaviviral Replication Complex: Coordination
444 between RNA Synthesis and 5′-RNA Capping. *Viruses* **7**, 4640-4656 (2015).
445 21. Developmental alterations in Huntington's disease neural cells and pharmacological rescue
446 in cells and mice. *Nat. Neurosci.* **20**, 648-660 (2017).
447 22. Jäger, S. *et al*. Purification and characterization of HIV-human protein complexes. *Methods*
448 **53**, 13-19 (2011).
449 23. Cox, J. *et al*. Accurate proteome-wide label-free quantification by delayed normalization and
450 maximal peptide ratio extraction, termed MaxLFQ. *Mol. Cell Proteomics* **13**, 2513-2526 (2014).
451 24. Cox, J. & Mann, M. MaxQuant enables high peptide identification rates, individualized
452 p.p.b.-range mass accuracies and proteome-wide protein quantification. *Nat. Biotechnol.* **26**,
453 1367-1372 (2008).

454 25. Teo, G. *et al*. SAINTq: Scoring protein-protein interactions in affinity purification - mass
455 spectrometry experiments with fragment or peptide intensity data. *Proteomics* **16**, 2238-2245
456 (2016).
457 26. Costes, S. V. *et al*. Automatic and quantitative measurement of protein-protein colocalization
458 in live cells. *Biophys. J.* **86**, 3993-4003 (2004).
459 27. Dunn, K. W., Kamocka, M. M. & McDonald, J. H. A practical guide to evaluating
460 colocalization in biological microscopy. *Am J Physiol Cell Physiol* **300**, C742 (2011).
461 28. Weger-Lucarelli, J. *et al*. Development and Characterization of Recombinant Virus
462 Generated from a New World Zika Virus Infectious Clone. *J. Virol.* **91** (2017).
463

Figure 1

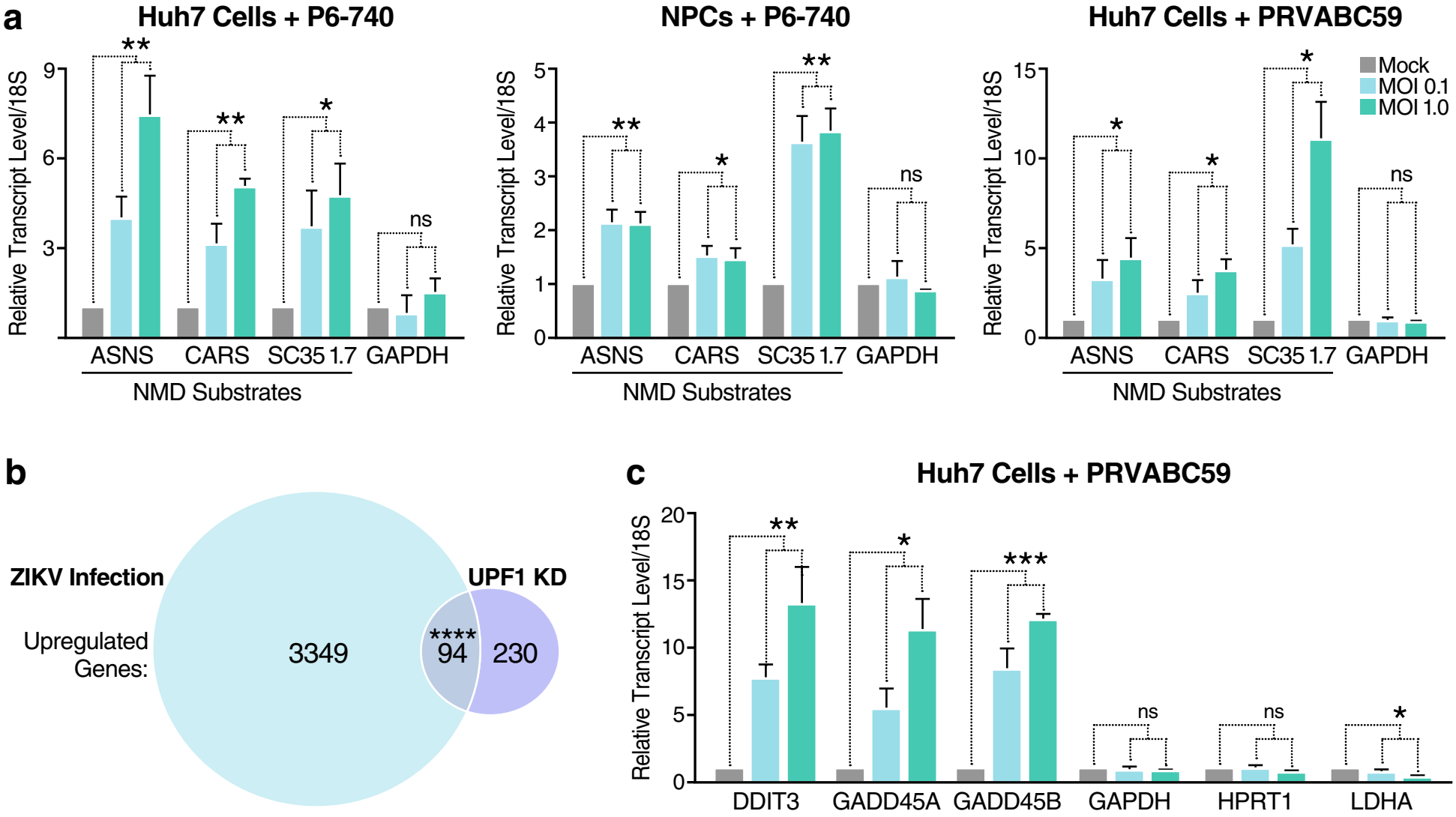
a
Huh7 Cells + P6-740
NPCs + P6-740
Huh7 Cells + PRVABC59
Relative Transcript Level/18S
Mock
MOI 0.1
MOI 1.0
ASNS
CARS
SC35 1.7
GAPDH
NMD Substrates
ns
b
ZIKV Infection
UPF1 KD
Upregulated Genes:
3349
****
94
230
c
Huh7 Cells + PRVABC59
Relative Transcript Level/18S
DDIT3
GADD45A
GADD45B
GAPDH
HPRT1
LDHA

Figure 2

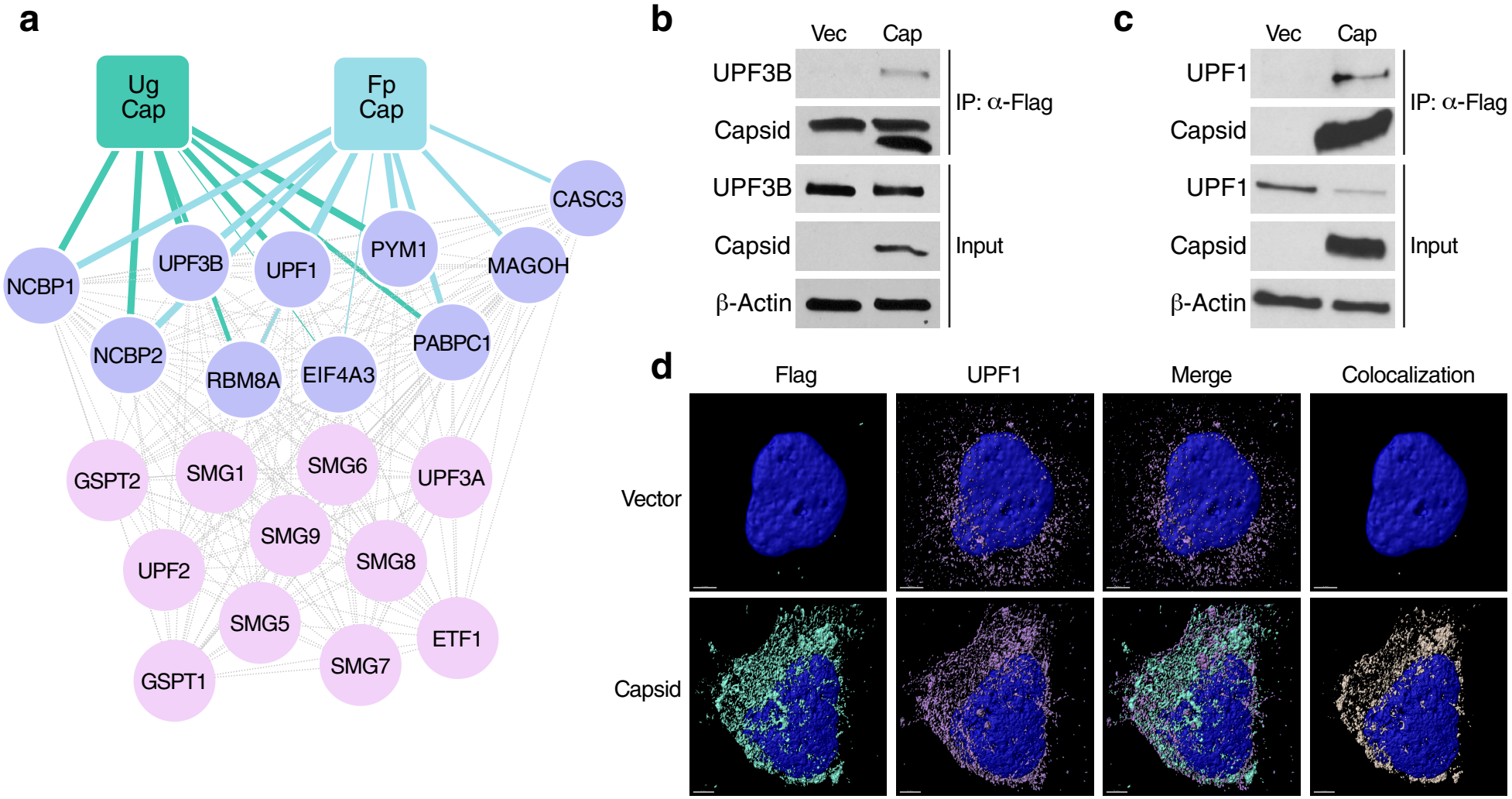
a
Ug Cap
Fp Cap
CASC3
NCBP1
UPF3B
UPF1
PYM1
MAGOH
NCBP2
RBM8A
EIF4A3
PABPC1
GSPT2
SMG1
SMG6
UPF3A
SMG9
SMG8
UPF2
SMG5
ETF1
SMG7
GSPT1
b
Vec
Cap
UPF3B
Capsid
IP: α-Flag
UPF3B
Capsid
Input
β-Actin
c
Vec
Cap
UPF1
Capsid
IP: α-Flag
UPF1
Capsid
Input
β-Actin
d
Flag
UPF1
Merge
Colocalization
Vector
Capsid

Figure 3

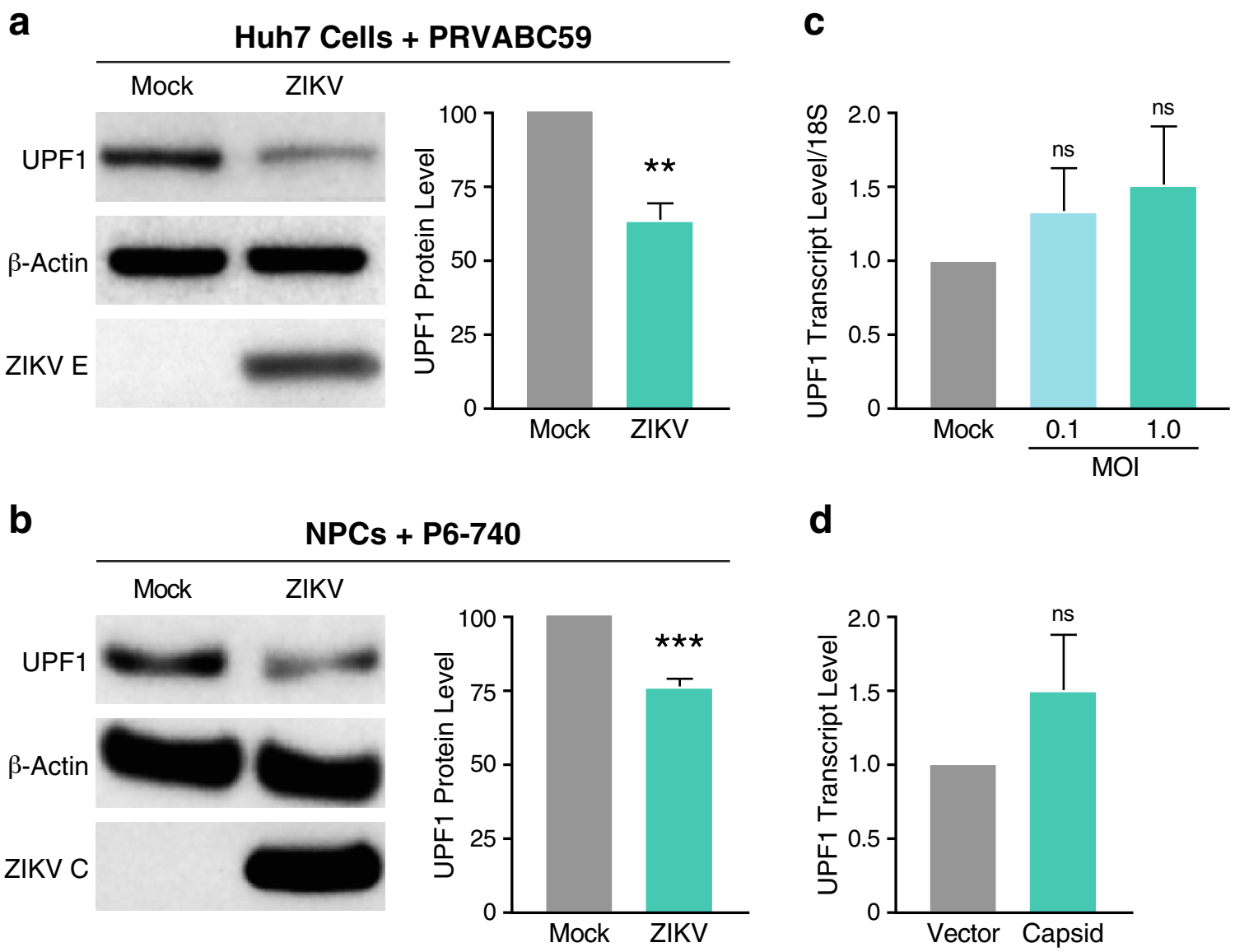
a
Huh7 Cells + PRVABC59
Mock
ZIKV
UPF1
β-Actin
ZIKV E
UPF1 Protein Level
100
75
50
25
0
**
Mock
ZIKV
b
NPCs + P6-740
Mock
ZIKV
UPF1
β-Actin
ZIKV C
UPF1 Protein Level
100
75
50
25
0
***
Mock
ZIKV
c
UPF1 Transcript Level/18S
2.0
1.5
1.0
0.5
0
ns
ns
Mock
0.1
1.0
MOI
d
UPF1 Transcript Level
2.0
1.5
1.0
0.5
0
ns
Vector
Capsid

Figure 4

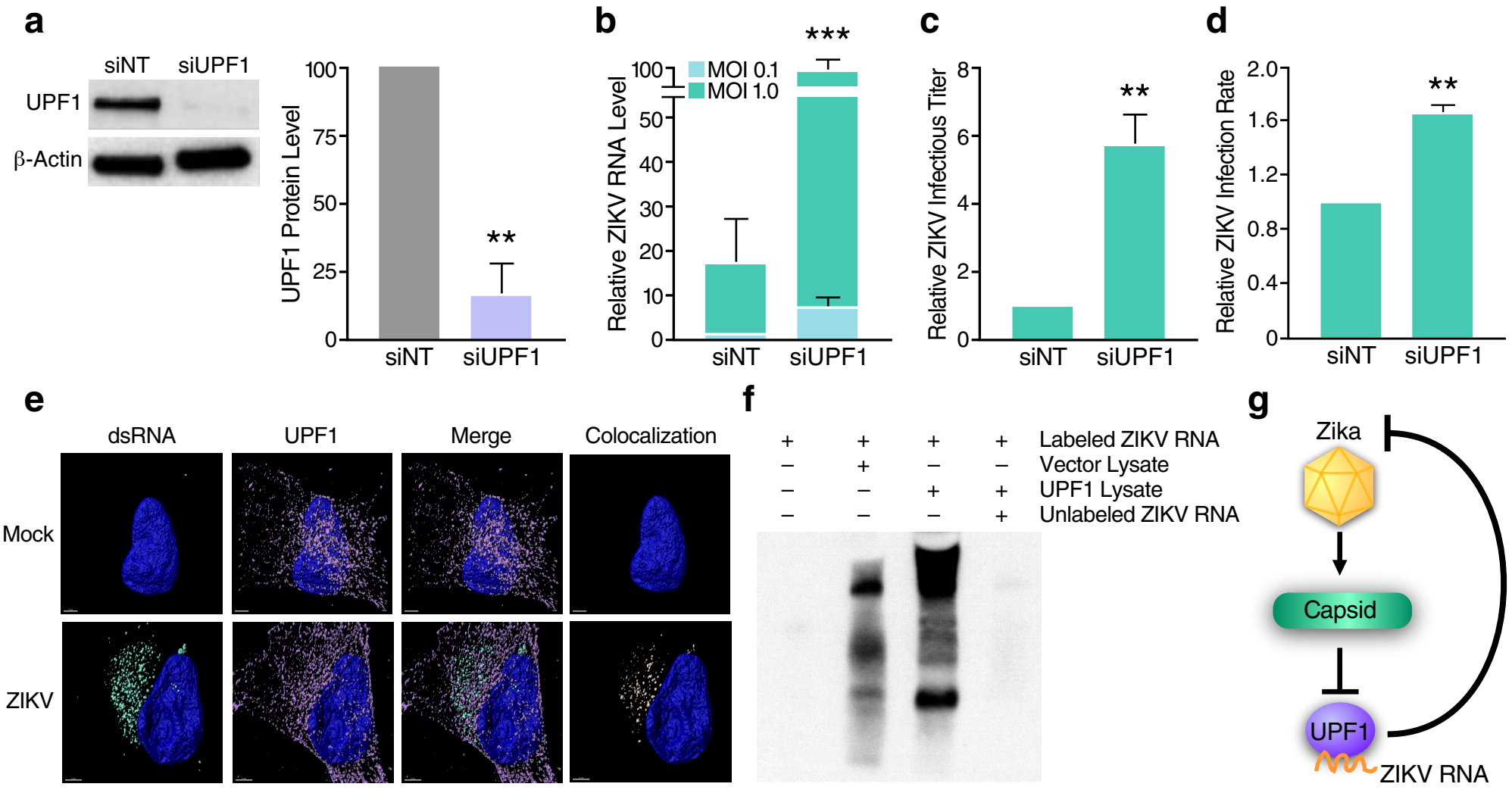
a
siNT
siUPF1
UPF1
β-Actin
UPF1 Protein Level
100
75
50
25
0
**
siNT
siUPF1
b
***
MOI 0.1
MOI 1.0
Relative ZIKV RNA Level
100
50
40
30
20
10
0
siNT
siUPF1
c
**
Relative ZIKV Infectious Titer
8
6
4
2
0
siNT
siUPF1
d
**
Relative ZIKV Infection Rate
2.0
1.6
1.2
0.8
0.4
0
siNT
siUPF1
e
dsRNA
UPF1
Merge
Colocalization
Mock
ZIKV
f
+ + + + Labeled ZIKV RNA
– + – – Vector Lysate
– – + + UPF1 Lysate
– – – + Unlabeled ZIKV RNA
g
Zika
Capsid
UPF1
ZIKV RNA